ACS APPLIED NANO MATERIALS

www.acsanm.org Article

AgAu Hollow Nanoshells on Layered Graphene Oxide and Silica Submicrospheres as Plasmonic Nanozymes for Light-Enhanced Electrochemical H_2O_2 Sensing

Rafael T. P. da Silva, Maria Paula de Souza Rodrigues, Gabriela F. B. Davilla, Adriano M. R. P. da Silva, André H. B. Dourado, and Susana I. Córdoba de Torresi*

Cite This: https://doi.org/10.1021/acsanm.1c02611 Read Online

ABSTRACT: Localized surface plasmon resonance (LSPR) is a phenomenon derived from the interaction between light and nanostructures, and its outcomes have been explored mainly for applications in surface-enhanced Raman spectroscopy (SERS), phototherapy, and catalysis. Bimetallic nanostructures are able to synergically combine the properties of two different metals to create a tuned response to LSPR according to their composition, shape, and morphology. In this study, an in situ synthesis of AgAu bimetallic hollow nanoshells (NS) over layered graphene oxide (GO) and silica submicrospheres (SiO_2) is presented. The synthesized structures acted as peroxidase-like nanozymes in the plasmon-enhanced electrochemical sensing of H_2O_2. The nanozymes were submitted to 405, 533, and 650 nm laser irradiation while performing the hydrogen peroxide reduction reaction (HPRR) with a fast response speed (4 s), exhibiting enhancements in sensitivity of 122% (for $Ag_{79}Au_{21}$/GO at 533 nm, 787 μA mM^{-1} cm^{-2}), 105% (for $Ag_{79}Au_{21}$/GO at 405 nm, 725 μA mM^{-1} cm^{-2}), and 119% (for $Ag_{50}Au_{50}/SiO_2$ at 650 nm, 885 μA mM^{-1} cm^{-2}) compared to the dark conditions when matching the LSPR band maximum for each synthesized structure. When laser stimuli did not match LSPR band maximum, lower enhancements were achieved in both cases. According to Michaelis–Menten enzyme kinetics, the nanozymes I_{max} followed the same LSPR bias and K_m^{app} was lowered after LSPR stimuli, showing the smallest values upon 405 nm irradiation (0.599 mM for $Ag_{79}Au_{21}$/GO and 0.228 mM for $Ag_{50}Au_{50}/SiO_2$) demonstrating increased substrate affinity in comparison to values previously reported in enzymatic and nonenzymatic biosensors of H_2O_2. Thus, we propose that LSPR is the main mechanism involved in the faster electron transfer rates and the consequent enhancement of electrochemical H_2O_2 sensitivities, I_{max}, and K_m^{app} by the bimetallic nanozymes synthesized by this approach.

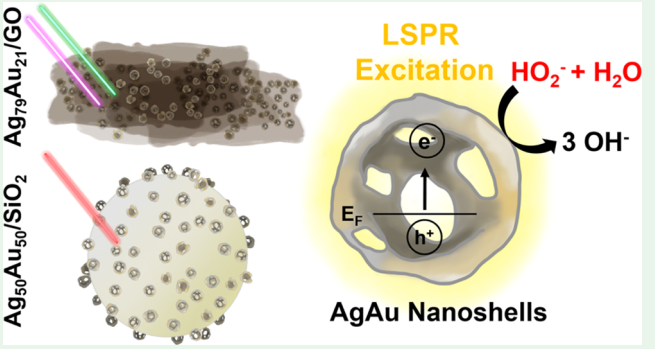

KEYWORDS: *nanoplasmonics, nanozymes, electrochemical sensors, LSPR, bimetallic nanoparticles*

INTRODUCTION

Hydrogen peroxide (H_2O_2) is an important analyte, and its determination plays a key role in different fields, such as biology, biomedicine, the food industry, and pharmaceutical, biochemical, and environmental analyses.[1,2] Moreover, it is involved in several biological processes, and its excess can affect the proper functioning of cells; thus, its accurate determination is valuable.[3] Over the years, different techniques have been explored for its determination, such as titrimetry,[4] chromatography,[5] spectrophotometry,[6] colorimetry,[7] fluorescence,[8] and electrochemistry.[9] However, electrochemical methods are preferred due to their rapid development, good accuracy, lower detection limits, easy miniaturization, biocompatibility, low cost, simple instrumentation, high selectivity, and fast response.[10−14]

Enzymatic and nonenzymatic electrochemical sensors are of great interest due to their high activities and selectivity. Nonetheless, enzymatic sensors have some disadvantages, such as poor stability, critical operating conditions, immobilization procedures, and limited lifetimes.[9,15] To overcome these challenges, nonenzymatic sensors using metallic nanoparticles (NPs) have been explored as an alternative for H_2O_2 sensing, acting as peroxidase-like catalysts.[13] Nanoparticles that

Received: August 21, 2021
Accepted: October 13, 2021

perform biocatalytic reactions in the replacement of enzymes have been called nanozymes in recent years.[16]

Metallic nanoparticles are of great interest in several areas due to their high surface area, quantum confinement effects, and localized surface plasmon resonance (LSPR) effects, which are not observed in their bulk counterparts.[17,18] The LSPR is a phenomenon that occurs mainly when the interaction between plasmonic metal nanostructures and irradiated light takes place. When the frequency of the light is resonant with the normal oscillation frequency of free electrons in these nanostructures, three major outcomes are reported: the formation of electron−hole pairs at the nanostructure surface, the local heat generated through the recombination of these pairs, and the near-field enhancement.[19] These effects have been extensively explored, including for catalysis,[20] photothermic therapy,[21] and surface-enhanced Raman spectroscopy (SERS).[22,23] Recently, the enhancement of electrochemical sensor sensitivity and responses through LSPR stimuli has been demonstrated to be an effective tool to improve sensitivity using a renewable source of energy.[24,25]

In particular, gold and silver have been extensively used as plasmonic sensors since they are noble metals with intense LSPR activity in the visible spectrum, mainly due to their dielectric functions in combination with the surrounding medium.[26] Silver nanoparticles (AgNPs) are advantageous as a result of their low rate of intrinsic energy loss with a high oscillator strength.[27] Although gold nanoparticles are more stable and inert than silver, they present higher rates of intrinsic energy loss, mainly in the short-wavelength regions, where interband transitions occur.[28]

The combination of more than one metal in bimetallic nanomaterials has attracted attention, as there is an opportunity not only to combine individual properties from the elements but also to achieve some unexpected properties arising from the synergy among them.[29−34] Typically, nanosized silver and gold are combined as core−shell or alloyed bimetallic nanoshells (NS).[29,30] Bimetallic hollow NS formed by the galvanic replacement reaction (GRR) have a considerable improvement in the ratio between the surface area and volume, minimizing the amount of metals.[35] Hollow nanostructures enhance plasmonic effects by forming plasmon hybridization between the cavity and sphere plasmon modes, inducing a more stable hybridized mode with improved charge separation on the structure.[36] In addition, the GRR between gold and silver progressively presents a redshift of the LSPR band depending on the corrosion level, which requires fewer energetic photons for plasmonic excitation than their individual metal counterparts.[37,38] There are still a few studies in the literature exploring AgAu hollow nanostructures to enhance electrochemical reactions, although none of them were found to use LSPR stimulus outcomes.[39−42]

Oxide supports have been used to stabilize the nanoparticles, preventing their aggregation through adhesion energy between the metals and the oxide surfaces.[43] In our study, we anchor metallic nanoparticles over layered graphene oxide (GO) and submicrospheres of silicon dioxide (SiO_2). Although GO-based nanocomposites present an insulating nature, they have been receiving attention in electrochemical sensing.[44,45] This is due to the fact that they offer a hydrophilic biocompatible microenvironment with an increased surface area that facilitates immobilization of electroactive species.[46] A second insulator, SiO_2 submicrosphere, was chosen in terms of comparison because it displays an assemble with increased exposition of nanoparticles. Besides, SiO_2 has been used in many fields such as biomedicine and catalysis as an inert host matrix of simple surface modification.[47−49]

In this work, we present an innovative in situ GRR between Au precursor and Ag templates anchored over GO and SiO_2 submicrospheres. The formed AgAu NS were evaluated as nanozymes in terms of their plasmonic catalytic activity toward the HPRR for H_2O_2 sensing to assess the aspects of LSPR with stimulation at specific wavelengths.

EXPERIMENTAL METHODS

Chemicals. Hydrogen tetrachloroaurate trihydrate ($HAuCl_4 \cdot 3H_2O$, 48% in gold, Sigma-Aldrich), silver nitrate ($AgNO_3$, ≥99%, Sigma-Aldrich), tetraethyl orthosilicate (TEOS, 98%, Sigma-Aldrich), ammonium hydroxide (NH_4OH, 27%, Synth), 3-aminopropylethoxysilane (APTES, ≥98%, Sigma-Aldrich), poly(vinylpyrrolidone) (PVP, Sigma-Aldrich, MW 55 000 and 10 000 g mol^{-1}), ethylene glycol ($C_2H_6O_2$, 99.5%, Synth), acetone (C_3H_6O, 99.5%, Synth), ethanol (C_2H_6O, 95%, Synth), toluene (C_7H_8, 100%, Synth), sulfuric acid (H_2SO_4, 98%, Synth), nitric acid (HNO_3, 65%, Synth), hydrochloric acid (HCl, 37%, Synth), phosphoric acid (H_3PO_4, 85%, Synth), potassium permanganate ($KMnO_4$, 100%, Synth), hydrogen peroxide (H_2O_2, 29%, Synth), potassium hydroxide (KOH, 90%, Sigma-Aldrich), graphite flakes (+100 mesh, Sigma-Aldrich), Carbon Vulcan (XC-72R), Nafion 5% ($C_7HF_{13}O_5S \cdot C_2F_4$, 15−20%, Sigma-Aldrich). All chemicals were analytical-grade reagents. Deionized water (18.2 MΩ) was used throughout the experiments.

Instrumentation. Scanning electron microscopy (SEM) images were obtained using a JEOL FEG-SEM JSM 6330F microscope operated at 5 kV. Samples were prepared by drop-casting an aqueous suspension of the particles on a Si wafer, followed by drying under ambient conditions. Transmission electron microscopy (TEM) images were obtained using a Tecnai FEI G20 operated at 200 kV. Samples were prepared by drop-casting 5 μL from an aqueous suspension of each sample in a lacey-carbon copper grid. UV−vis spectra were obtained using a Shimadzu UV-2600 UV−vis spectrophotometer and quartz cuvette with an optical path of 1 cm. For each measurement, the cuvette was washed three times with acetone and once with water. To determine the metal composition in the samples, ICP-OES Spectro Arcos equipment was used. The digestion of the samples occurred by aqua regia in a 1:1 ratio. Then, a 10-fold dilution with distilled water was performed before each measurement. The X-ray diffraction (XRD) data were obtained using Rigaku-Miniflex equipment and Cu Kα radiation. The diffraction pattern was measured in the 2θ range of 10−70° with a 1° min^{-1} angular speed scan. X-ray photoelectron spectroscopy (XPS) was performed in a Specs FlexPS system equipped with a Phoibos 150 2D CCD detector and using an XR50 X-ray source with a nonmonochromatized Al Kα (1486.61 eV) source. The catalyst ink was drop-cast over a Si substrate, covering properly the Si surface, as no Si signal (main transition for SiO_2 is Si 2p at 103.3 eV)[50] was detected. All spectra were registered in a high-vacuum chamber at pressures below 10^{-9} mbar and were corrected by the C 1s signal (284.5 eV).[50,51]

Silver Nanoparticle (AgNP) Synthesis via the Ethylene Glycol Method. As previously described, 5.0 g of PVP with an MW of 10 000 was dissolved in 37.5 mL of ethylene glycol at room temperature.[52] Then, 200 mg of $AgNO_3$ was solubilized with assistance from an ultrasonic bath. The system was heated by a heating plate with magnetic stirring at a 1 °C min^{-1} rate until 120 °C and left reacting for 90 min. After cooling, the product was diluted with distilled water to 125 mL.

AgAu Nanoshell (AgAu NS) Synthesis. Inspired by a previously described procedure,[35] a solution of PVP with an MW of 55 000 (50 mL, 1 mg mL^{-1}) was heated to ebullition by a heating plate with a magnetic stirrer, and 2.78 mL of AgNPs was added. After 10 min, 5, 10, 20, or 30 mL of $HAuCl_4 \cdot 3H_2O$ (0.2 mmol L^{-1}) was added dropwise for the galvanic replacement reaction to take place. Then, the reaction was stirred for 10 min to be completed. The amount of

https://doi.org/10.1021/acsanm.1c02611
ACS Appl. Nano Mater. XXXX, XXX, XXX−XXX

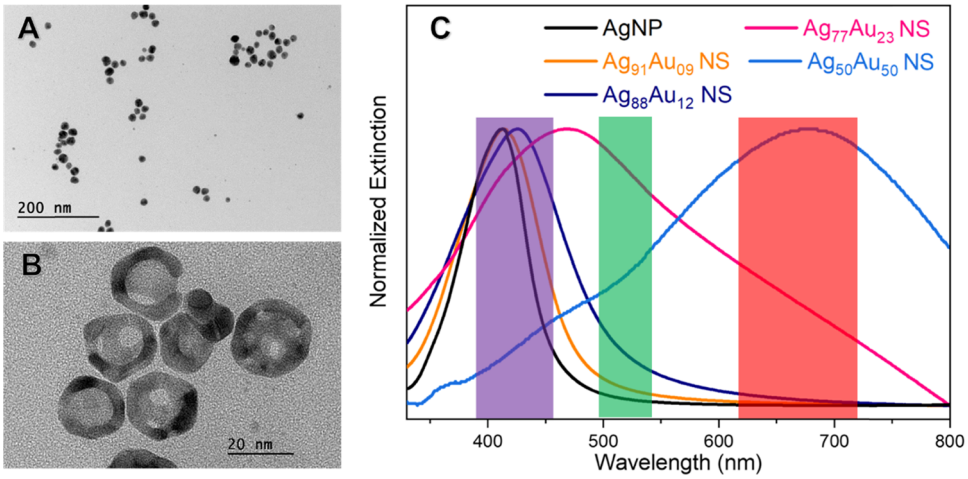

Figure 1. Characterization of AgAu NS synthesis. TEM micrographs for AgNPs (A) employed as templates for the synthesis of $Ag_{50}Au_{50}$ NS with hollow interiors (B). UV−Vis spectra for AgNPs and different degrees of galvanization of AgAu NS, represented by the metal ratio in the subscript (C). The subscription in the caption represents the molar ratio between the metals, and the colored stripes represent the absorbed colors corresponding to that spectral region.

$HAuCl_4{\cdot}3H_2O$ (0.2 mmol L^{-1}) dictated the degree of corrosion of the structure, as depicted by the structural characterization.

Graphene Oxide (GO) Synthesis. A modified Hummer's method was used as previously described in the literature.[53] Therefore, a mixture of 360 mL of H_2SO_4 and 40 mL of H_3PO_4 was prepared. To this mixture, a solid mixture of 18.0 g of $KMnO_4$ in six equally divided portions and 3.0 g of graphite was added to an ice-cold bath. The resulting solution was stirred for 12 h at 50 °C on a stirring hot plate. Then, 3 mL of H_2O_2 (30 v/v) and 400 mL of frozen distilled water were added. The product was vacuum-filtered and washed with a mixture of 1020 mL of distilled water, 180 mL of HCl, and 600 mL of ethanol. The resulting material was left to dry at 70 °C for 12 h.

Amine-Functionalized Submicrospheres of Silicon Dioxide (SiO_2) Synthesis. A modified Stöber method was used for the synthesis of SiO_2-NH_2.[47] A mixture containing 35 mL of NH_4OH, 75 mL of ethanol, and 15 mL of distilled water was added to 25 mL of a solution of TEOS in ethanol (26% v/v) and stirred for 2 h. The submicrospheres were separated by centrifugation (7000 rpm, 10 min) and washed twice with distilled water and once with ethanol. The sample was dried at 100 °C and calcinated at 600 °C for 2 h. The amine functionalization procedure was performed with some adjustments from that previously described.[54] Surface functionalization promoted an optimized anchoring platform to metallic nanoparticles compared to nonfunctionalized synthesis. Therefore, 1 g of SiO_2 submicrospheres was added to 150 mL of dried toluene and sonicated for 30 min. Then, 1.5 mL of 3-aminopropylethoxysilane (APTES) was added dropwise to the mixture under stirring at room temperature and kept under stirring for 2 h. Finally, SiO_2-NH_2 was separated by centrifugation, washed once with toluene and twice with acetone, and dried at 80 °C for 20 h.

Synthesis of AgNP/GO and AgNP/SiO_2. To decorate GO and SiO_2 with AgNPs, a dry impregnation method was used. Therefore, 10 mL of the as-synthesized AgNPs was washed three times in a mixture of 10% water and 90% acetone for 15 min at 15 000 rpm. Some droplets of water were used to disperse the pellet, and 10 mL of acetone was further added to remove the excess PVP used in the AgNP synthesis. This procedure was performed three times. The final redispersion was performed with 1 mL from a 1:1 mixture of water and ethanol. Then, 200 mg of solid GO or SiO_2-NH_2 was spread onto a petri dish over a heating plate set at 60 °C. Aliquots of 70 μL were sequentially dropped with a micropipette onto the solid, and with the help of a spatula, the solid was homogenized until completely dried. This process was repeated until the concentrated 1 mL was entirely consumed.

Synthesis of AgAu/GO and AgAu/SiO_2. The galvanic replacement reaction proceeded for the in situ formation of AgAu NS. Therefore, 10 mg of AgNP/GO or AgNP/SiO_2 was added to 8.4 mL of an aqueous solution of PVP with an MW of 55 000 (1 mg mL^{-1}) brought to boil on a heating plate with magnetic stirring. After complete suspension, 1 mL of $HAuCl_4{\cdot}3H_2O$ (0.2 mmol L^{-1}) was added dropwise. Then, the reaction was stirred for an additional 10 min for completion.

Ink Preparation. For further electrochemical application, the catalysts were deposited on Carbon Vulcan by wet impregnation. Five milliliters of each catalyst and 5 mg of Carbon Vulcan were dispersed in water. The mixture was sonicated for 1 h and stored for further experiments.

Electrochemical Methods. A three-electrode electrochemical cell was used for the electrochemical experiments, with Ag/AgCl (KCl saturated) as a reference electrode and Pt wire as the auxiliary electrode. The working electrode was a glassy carbon rotating-disk electrode (GCE, d = 1.5 mm) modified by drop-casting 10 μL of the previously prepared catalyst ink and 5 μL of Nafion 0.05%. Moreover, 70 mL of 1.0 mol L^{-1} KOH solution was used as the electrolyte. The cell was N_2-saturated to avoid reactive oxygen species formation. Hydrodynamic conditions (1600 rpm, controlled by a Pine AFMSRCE RDE) were used to keep the analyte concentration (H_2O_2) homogeneous in the electrochemical cell.

Triangular and current step perturbations were controlled and executed by a PGSTAT302N Autolab potentiostat/galvanostat to investigate the catalyst H_2O_2 sensing performance. All perturbation programs are depicted in the figures. For the current step perturbation investigation, a fixed potential of −0.3 $V_{Ag/AgCl}$ was applied for 5 min, followed by 20 additions of 50 μmol L^{-1} H_2O_2 and 5 additions of 100 μmol L^{-1} H_2O_2. The additions were made every 20 s.

For the light experiments, 200 mW modular lasers of 405, 533, and 650 nm were positioned 7 cm from the working electrode. The laser was turned on at least 5 min before the measurements, avoiding possible fluctuations in power. The triangular and step perturbations were performed as described previously for the light experiments. All measurements were normalized by the electrochemically active surface area (ECSA), which was estimated from the double-layer capacitance (C_{dl}) of each catalyst divided by the C_{dl} of bare Carbon Vulcan.

RESULTS AND DISCUSSION

Synthesis of AgAu Nanoshells (AgAu NS). The synthesis of AgAu NS was proceeded by the galvanic replacement reaction (GRR), a strategy that has been used

https://doi.org/10.1021/acsanm.1c02611
ACS Appl. Nano Mater. XXXX, XXX, XXX−XXX

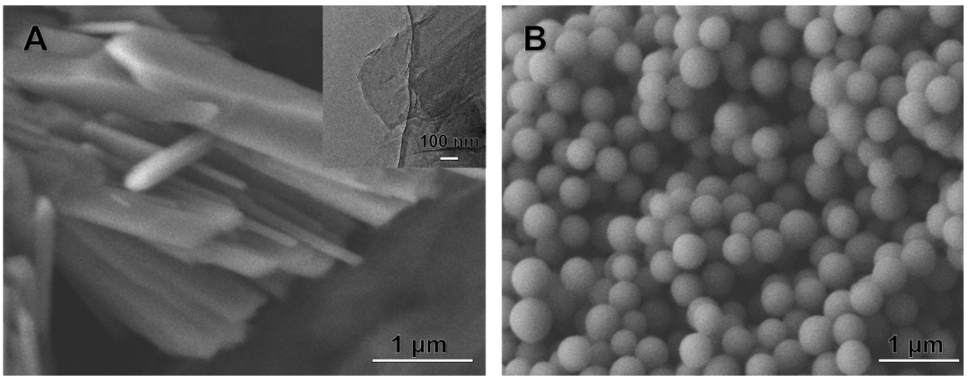

Figure 2. Micrographs of the supports. SEM micrograph of GO with a TEM micrograph as the inset (A) and SEM micrograph of SiO_2 submicrospheres (B).

in the field of nanoparticles design to create hollow nanostructures with tunable and well-controlled physical and chemical properties.[55,56] In this study, AgNPs were synthesized by the ethylene glycol method as templates and $HAuCl_4$ as the gold precursor. Different degrees of galvanization were achieved by varying the amount of gold precursor added from 5 to 30 mL of $HAuCl_4 \cdot 3H_2O$ (0.2 mmol L^{-1}). The molar ratio among the two metals was determined by ICP-OES and is represented as a subscript in the "AgAu NS" notation: $Ag_{91}Au_{09}$, $Ag_{88}Au_{12}$, $Ag_{77}Au_{23}$, and $Ag_{50}Au_{50}$ NS. TEM micrographs from the templates and the resultant $Ag_{50}Au_{50}$ NS after GRR are presented in Figure 1A,B, respectively. The size distribution before and after GRR for this sample is represented in Figure S1. The AgNP templates presented a spherical shape of 16 ± 3 nm in diameter, whereas after the GRR, the $Ag_{50}Au_{50}$ NS followed a spherical shape with hollow interiors with a diameter of 20 ± 4 nm and a shell thickness of ~4 nm. Both samples were relatively monodispersed in terms of size and morphology. TEM images of $Ag_{91}Au_{09}$ and $Ag_{77}Au_{23}$ are demonstrated in Figure S2, where a progressive corrosion degree is noticeable, starting from a bulky nanostructure with some defects (Figure S2A, $Ag_{91}Au_{09}$) toward a thicker shell structure presented by $Ag_{77}Au_{23}$ (Figure S2B). Figure S3 shows HRTEM images of $Ag_{50}Au_{50}$ NS, confirming the presence of 0.234 nm (111) lattice spacing after averaging the distance of 15 fringes. This can be assigned to the presence of fcc of either Ag or Au (ICSD 98-004-4362 and 98-004-4387). The center of the particle focused in HRTEM shows no fringes, indicating the hollow interior of the formed nanostructure. Energy-dispersive spectroscopy (TEM-EDS) was performed over the same particle, indicating the coexistent presence of both Ag and Au. Figure 1C shows the UV−Vis absorption spectra of the different materials and reveals that while the AgNP templates had their maximum at 413 nm, represented by a narrow LSPR band, bimetallic AgAu NS samples varied their maximum and presented band broadening. The bands were centered at 413 nm for $Ag_{91}Au_{09}$ NS, 425 nm for $Ag_{88}Au_{12}$ NS, 469 nm for $Ag_{77}Au_{23}$ NS, and 678 nm for $Ag_{50}Au_{50}$ NS with a progressive LSPR band redshift and broadening. The colored stripes on the UV−Vis extinction spectra represent the absorbed colors corresponding to that spectral region.

Both the redshift and broadening of the LSPR band are in agreement with the increase in the Au ratio in the alloy and the expected degree of corrosion resulting from the sequence of GRR.[32,38,57] The red-shifted LSPR band toward the near-infrared (NIR) region has been demonstrated by previous studies to be an interesting property concerning biological applications related to maximized penetration in tissue, such as photodynamic therapy.[58,59] Moreover, the LSPR excitation of the red-shifted alloy requires lower-energy photons than the pure silver or gold nanoparticle counterparts with higher-energy LSPR bands. In addition, band broadening provides the opportunity to work with wider spectrum sources, such as the solar light spectrum, with higher efficiency yields concerning plasmonic outcome effects.[60]

In Situ Synthesis of AgAu NS over Graphene Oxide and SiO_2 Submicrospheres (AgAu/GO and AgAu/SiO_2). Two supports were chosen for the in situ synthesis of AgAu NS. The first is graphene oxide (GO), a layered organization of carbon functionalized with hydroxyl groups, and the second is SiO_2, a submicrometric material with a spherical shape functionalized with amine groups. The synthesis of GO followed an improved Hummer's method, where the flake graphite is exfoliated by a strong oxidizing mixture up to its conversion to graphene oxide.[53] In turn, submicrospheres of SiO_2 were synthesized by a slightly modified Stöber's method with post-functionalization with APTES, with an amine terminal group that improves the anchoring of further synthesized metallic nanoparticles.[61] Micrographs of the supports are shown in Figure 2. GO presented a layered structure, and its Raman spectrum analysis suggests Raman modes D (1353 cm^{-1}), 2D (2670 cm^{-1}), and G (1595 cm^{-1}), as indicated in Figure S4. X-ray diffraction (XRD) patterns of both supports are demonstrated in Figure S5. SiO_2 submicrospheres show a typical amorphous peak, whereas graphene oxide shows a typical main peak at 2θ = 9.3°, indicating (001) planes with 0.95 nm interlayer spacing, according to Bragg's law.[62] The weak peaks at 2θ = 23.0 and 42.6° may indicate incomplete oxidation of graphite.[63,64] Concerning the particle size distribution, SiO_2 submicrospheres have a relatively monodisperse distribution of 367 ± 39 nm in diameter, as indicated by the histogram in Figure S1.

To perform the in situ GRR, the supports were impregnated with AgNPs in a first step, as shown by the TEM micrographs in Figure 3A,B. The AgNPs maintained their original spherical shape after the impregnation process, and their distribution along the sample was homogeneous, apart from some clusters over the SiO_2 microspheres, especially between the particles. The opacity of AgNPs in GO sheets may indicate either an uneven surface of GO or an overlap of graphene sheets in the preparation of TEM grid, since AgNP probably would not be

https://doi.org/10.1021/acsanm.1c02611
ACS Appl. Nano Mater. XXXX, XXX, XXX−XXX

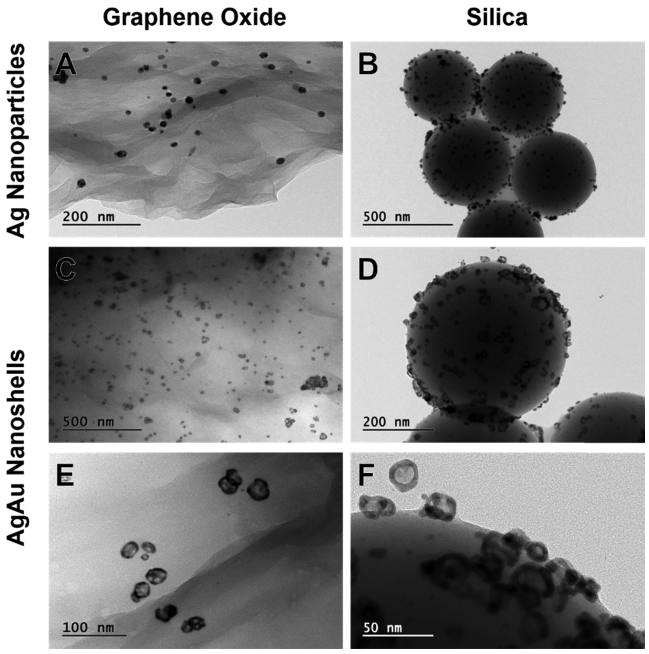

Figure 3. TEM characterization of the in situ synthesis of AgAu NS. TEM micrographs of AgNPs over GO (A) and over SiO_2 submicrospheres (B). After an in situ galvanic replacement reaction, TEM micrograph of $Ag_{79}Au_{21}$/GO, (C), also represented by the micrograph of higher magnification (E) and $Ag_{50}Au_{50}/SiO_2$ (D), with the respective micrograph of higher magnification (F) were obtained.

able to interpenetrate GO layers. The GRR took place in situ, that is, between Ag^0, from the supported AgNPs, and Au^{3+}, from the gold precursor added. The AgAu NS in GO and SiO_2 are shown in Figure 3C,D, respectively. Higher magnifications of the formed structures are represented in Figure 3E,F. Concerning the formation of the AgAu NS, both materials presented a similar morphology compared with the free $Ag_{50}Au_{50}$ NS (Figure 1), that is, a hollow interior of a perforated metallic nanoshell. Nonetheless, as determined by ICP-OES, the NS showed different compositions on each support, $Ag_{79}Au_{21}$/GO and $Ag_{50}Au_{50}/SiO_2$. In comparison, the shells of $Ag_{79}Au_{21}$/GO presented better monodispersion and uniformity throughout the sample, whereas some larger NS and agglomerates resided on $Ag_{50}Au_{50}/SiO_2$. Anchored on the supports, AgAu NS show a considerable improvement in the sample stability, since after a couple of days free AgAu nanoshells lost their original grayish color and a precipitated was observed in the bottom of the conical centrifuge tubes, whereas no significant difference was observed after at least 1 month in the TEM images of supported samples on GO and/or SiO_2, although mixing was required due to sedimentation. Figure S1 shows the histograms of the formed AgAu NS on each support. Although a composition discrepancy was found between the two samples, there was no evident difference in corrosion levels in the TEM images. This result indicates that although the same amount of precursor was added in the synthesis, GRR occurred in higher yields in the $Ag_{50}Au_{50}/SiO_2$ sample, possibly due to the limited access of precursor between the GO layers or the adsorption of Au^{3+} on the high surface area of GO layers. Moreover, a distinct plasmonic behavior toward the plasmon-enhanced HPRR is expected in each case, as different corrosion levels lead to distinct LSPR band shapes and positions, as demonstrated in Figure 1C. Scheme 1 summarizes the routes used for the in situ production of AgAu/GO and AgAu/SiO_2.

These materials were also analyzed by XPS (Figure S6). The Au and Ag signals in the survey measurements are much lower than the ones observed for the other elements, which is related to the low amount of these elements in the catalyst ink composition. The Ag signals related to the Ag_{3d} transition were observed at 367.7 and 373.5 eV for the GO supported material, and 366.8 and 372.2 eV for the SiO_2. The distance between these peaks is always close to 6 eV, being 5.8 and 5.4 eV for GO and SiO_2, respectively. With these relations, it is possible to assign these signals to the presence of Ag^0 in the material.[50] In both cases, the signal located at lower binding energies is always broader than that located at higher binding energies. This can indicate the presence of Ag^+, to some extent, but due to the low signal-to-noise ratio observed, a deconvolution could not be performed.[65,66]

For the Au_{4f} signals, the intensity was very low and the proximity to the Si 2p signals made the analysis more difficult. In this case, we decided to discuss just the Au $4f_{7/2}$, since the signals which should be related to Au $4f_{5/2}$ were too broad to be distinguished from the baseline in the case of the SiO_2 supported material. In both cases, GO and SiO_2 supported materials, the signal was found to be centered at 82.8 eV. This signal is lower than the 84.0 eV expected for Au^0.[50] This difference can be related to the cluster-sized material, which already lead to works reporting Au^0-related signals between 82.6 and 83.1 eV.[65,67,68]

Electrochemical Characterization. After material synthesis and characterization, we focused on their application as

Scheme 1. Schematic Representation of the Routes for In Situ GRR Leading to the Formation of AgAu/GO and AgAu/SiO_2

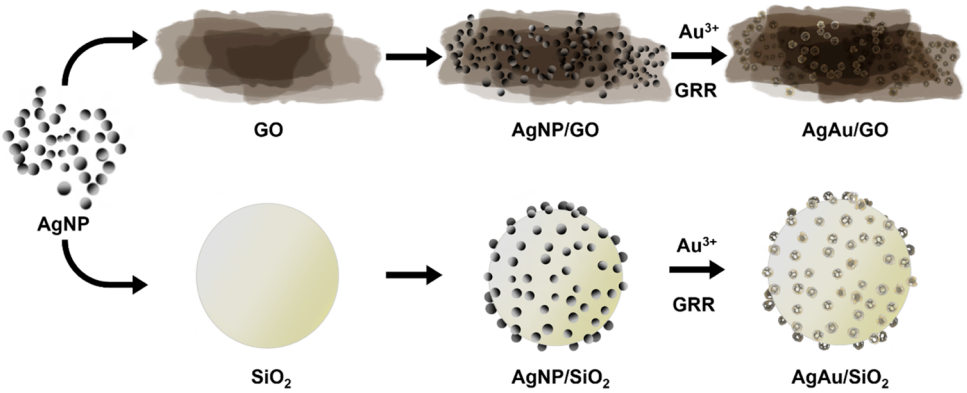

https://doi.org/10.1021/acsanm.1c02611
ACS Appl. Nano Mater. XXXX, XXX, XXX−XXX

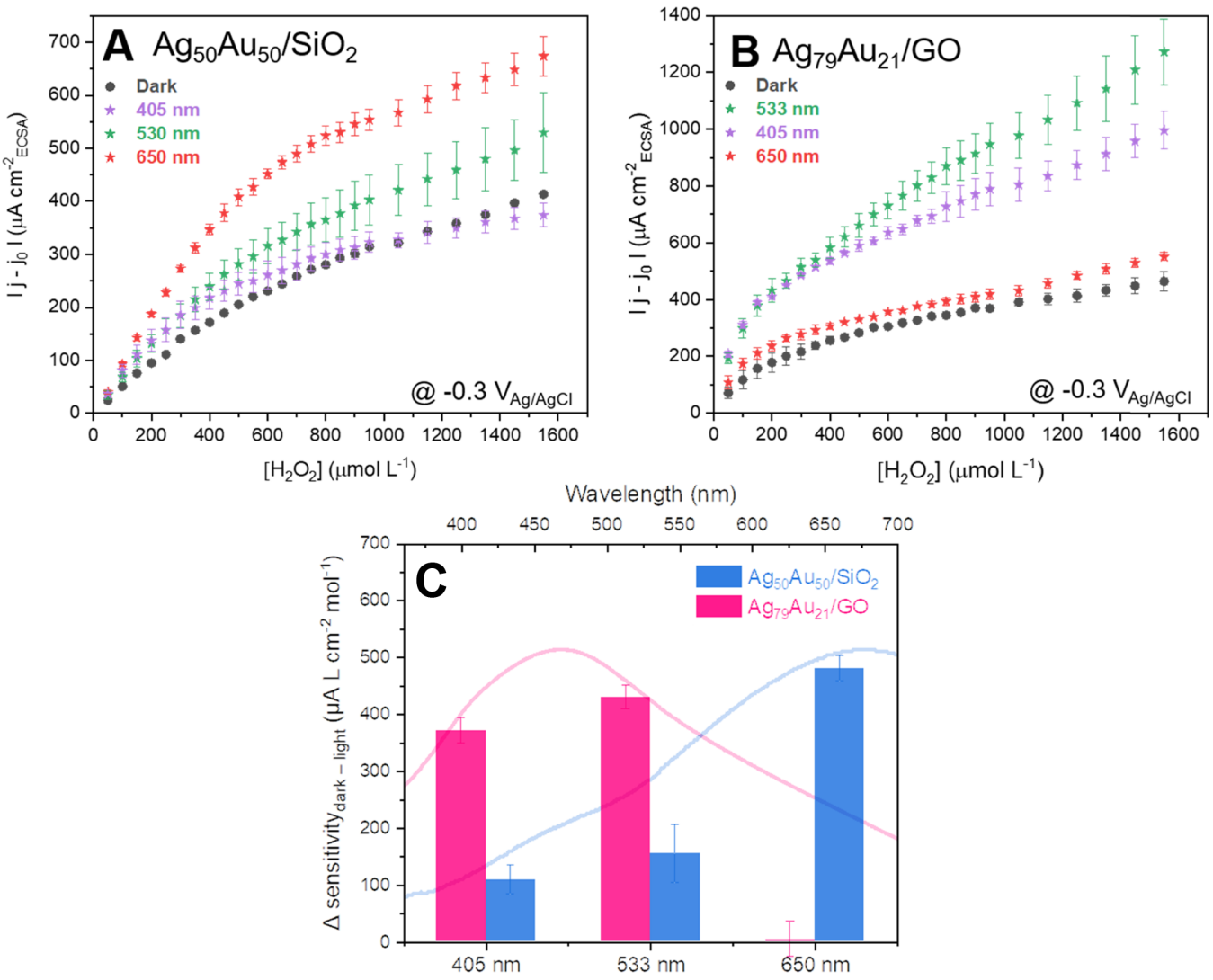

Figure 4. Calibration curve for the HPRR by $Ag_{50}Au_{50}/SiO_2$ (A) and $Ag_{79}Au_{21}/GO$ (B) under irradiation by a set of lasers. UV−vis spectra of $Ag_{50}Au_{50}/SiO_2$ and $Ag_{79}Au_{21}/GO$ and the difference in sensitivity bar graph with and without each laser source incidence (C). All measurements were performed at −0.3 $V_{Ag/AgCl}$ in KOH 1.0 mol L^{-1}.

nanozymes for plasmon-enhanced H_2O_2 electroreduction and sensing. We are interested in evaluating the differences in the plasmonic properties of $Ag_{50}Au_{50}/SiO_2$ and $Ag_{79}Au_{21}/GO$ toward the enhancement of the HPRR under different wavelengths within the visible light spectrum. We started by performing triangular potential sweeps at 100 mV s^{-1} from 0.3 to −0.4 $V_{Ag/AgCl}$, which is the potential range for H_2O_2 reduction in alkaline media.[69,70] They were performed before and after H_2O_2 addition for the bare supports before and after AgAu NS formation (Figure S7). It is noteworthy that the bare supports only show current due to impregnation in Carbon Vulcan, as both GO and SiO_2 present insulant behavior.

Bare SiO_2 (Figure S7A) showed no oxidation and/or reduction peaks in the cyclic voltammetry. On the other hand, SiO_2 modified with AgAu NS presented an increase in current, indicating a higher conductivity due to metallic loading. After H_2O_2 addition to $Ag_{50}Au_{50}/SiO_2$, the catalyst showed an increase in current density, starting at −0.20 $V_{Ag/AgCl}$, typical from the HPRR.[71,72] Bare GO and $Ag_{79}Au_{21}/GO$ showed no characteristic peaks in the cyclic voltammetry (Figure S7B). Nonetheless, the addition of the analyte $Ag_{79}Au_{21}/GO$ improved the current density toward HPRR. Thus, in both cases, for SiO_2 and GO, the supports presented a low contribution toward the HPRR and required a catalytic counterpart to perform this reaction.

Although both materials showed improved activity, $Ag_{79}Au_{21}/GO$ presented a more capacitive electrochemical profile and lower current density than $Ag_{50}Au_{50}/SiO_2$. To assess this subject, electrochemical impedance spectroscopy (EIS) experiments were performed with bare SiO_2 and GO (Figure S8). The charge transfer resistance (R_{ct}) was obtained from the diameter of the semicircle in the Nyquist plot.[73,74] A lower R_{ct} indicates a higher rate of electron transfer kinetics and, consequently, a higher activity.[75−77] Neither of the measured Nyquist plots presented a closed semicircle, meaning that both materials present expressive isolation properties and low faradaic activity at the applied potential.[78] However, GO signal seems to present not only a tendency to close the semicircle at higher real values (R_{ct}) but also higher $-Z''$ values, which can indicate higher capacitive behavior, if a capacitor in parallel to a resistor (double-layer capacitance and R_{ct}, respectively) is assumed as an electrochemical equivalent circuit.

https://doi.org/10.1021/acsanm.1c02611
ACS Appl. Nano Mater. XXXX, XXX, XXX−XXX

Plasmon-enhanced sensing for H_2O_2 detection was investigated by monitoring the catalyst chronoamperometric response at −0.3 $V_{Ag/AgCl}$ with and without light incidence (Figure S9). We worked with modular lasers as a proof of concept to evaluate the LSPR outcome effects, as this is a wavelength-dependent property. Three wavelengths were chosen, according to the maximum LSPR absorption of each AgAu stoichiometric ratio as depicted in Figure 1C: 405 and 533 nm, located in the maximum LSPR absorption from a free structure close to $Ag_{79}Au_{21}$/GO composition, and 650 nm, matching the maximum intensity of the free $Ag_{50}Au_{50}$ LSPR band. The chronoamperometric response was recorded for the clean GCE, bare SiO_2 and GO, and AgAu NS-modified supports.

Before analyte addition, the current reached a steady state, and as hydrogen peroxide solution was added, the current increased proportionally. The calibration curves were derived from the linear step perturbation (Figure S9) and are shown in Figure 4. Negligible activity toward hydrogen peroxide reduction was observed for the GCE, GO, and SiO_2 electrodes, even under light irradiation, as shown in Figure S10. Nonetheless, the supports modified with AgAu NS increased the activity sharply with light, indicated by the rapid increase in current density.

Both the $Ag_{50}Au_{50}/SiO_2$ and $Ag_{79}Au_{21}$/GO electrodes showed a fast response to each H_2O_2 addition, achieving a steady-state current within 4 s after each aliquot. A fast response indicates rapid diffusion, which can be facilitated by hydrodynamic conditions.[24] The $Ag_{50}Au_{50}/SiO_2$ analytic curve showed two linear ranges (Figure 4A), the first from 0 to 600 μmol L^{-1} H_2O_2 and the second from 600 μmol L^{-1} onward. $Ag_{79}Au_{21}$/GO calibration curves (Figure 4B) also showed two linear ranges, the first from 0 to 300 μmol L^{-1} and the second from 300 μmol L^{-1} onward. $Ag_{50}Au_{50}/SiO_2$ and $Ag_{79}Au_{21}$/GO showed similar responses under dark conditions, with sensitivities of 404 and 353 μA mM^{-1} cm^{-2}, respectively. The similar sensitivity under dark conditions and the poor response of the bare supports (Figure S10) indicate that NS are primarily responsible for the observed electrocatalytic reaction, acting as nanozymes in the HPRR.

$Ag_{50}Au_{50}/SiO_2$ achieved the highest sensitivity, considering both the first and second linear ranges, under 650 nm laser incidence. The slope concerning the first range indicates a sensitivity of 885 μA mM^{-1} cm^{-2}, with a 119% increase with respect to the dark condition (Figure 4C). Both 405 and 533 nm lasers showed similar and worse responses, with increases of 27 and 38% in sensitivity relative to the condition without light, respectively. This result agrees with the NS LPSR band, as both 405 and 533 nm are on the tail of the LSPR band for the structure with equal metal ratios ($Ag_{50}Au_{50}$ NS) and present only suboptimal improved activity. On the other hand, 650 nm is located at the maximum of the LSPR extinction band, leading to an optimal response (Figure 1C). $Ag_{79}Au_{21}$/GO calibration curves showed its highest response under 533 nm laser irradiation, 787 μA mM^{-1} cm^{-2}, representing a 122% increase under light incidence, followed by a 105% increase with a 405 nm laser. As seen in the LSPR spectra of $Ag_{77}Au_{23}$ NS, the sample with the closest composition to $Ag_{79}Au_{21}$/GO, at both 405 and 533 nm, shows similar LSPR intensities, explaining the observed behavior. The 650 nm laser showed the poorest improvement with light irradiation (1.08%) for these electrodes. Sensitivities for each material and experiment are summarized in Table 1.

Table 1. Linear Fit from the First Slope of Calibration Curves and Kinetic Parameters according to Michaelis−Menten Enzyme Kinetics for the Nanozymes

catalyst	light source	linear fit	I_{max} (μA cm^{-2})	K_m^{app} (mM)
$Ag_{50}Au_{50}/SiO_2$	dark	$y = 0.404x + 6.41$, $R^2 = 0.997$	743.1	1.327
	405 nm	$y = 0.513x + 13.0$, $R^2 = 0.980$	521.7	0.599
	533 nm	$y = 0.559x + 12.0$, $R^2 = 0.993$	898.0	1.147
	650 nm	$y = 0.885x + 3.93$, $R^2 = 0.995$	1177	1.021
$Ag_{79}Au_{21}$/GO	dark	$y = 0.353x + 108$, $R^2 = 0.986$	568.7	0.506
	405 nm	$y = 0.725x + 303$, $R^2 = 0.981$	864.7	0.228
	533 nm	$y = 0.787x + 269$, $R^2 = 0.995$	1405	0.506
	650 nm	$y = 0.350x + 164$, $R^2 = 0.976$	541.4	0.324

In both cases, the enhancement in sensitivity is wavelength-dependent, with the maximum increase with light following the trends observed in the LSPR extinction spectra for NS with the corresponding composition. Thus, for $Ag_{50}Au_{50}/SiO_2$ and $Ag_{79}Au_{21}$/GO, the plasmonic effect led to an improvement toward the HPRR. The sensitivities found for our synthesized nanozymes under dark conditions are in agreement with the best materials performing the same reaction in previous studies.[79] However, with an enhancement of ∼120% under light exposure, our sensor demonstrated excellent performance in comparison to previously reported nanozymes.

The enzyme-like activity of nanozymes are usually carried out through Michaelis−Menten enzyme kinetics.[16,80] In our study, this strategy was used to determine the maximum response current (I_{max}) and the apparent Michaelis constant (K_m^{app}) of the designed nanozymes as demonstrated in Table 1. The hyperbolic response of peroxide concentration and the amperometric signals are in agreement with the Michaelis−Menten kinetics and can be described according to the hyperbolic function $y = ax/(b + x)$, where a corresponds to I_{max} and b to K_m^{app}.[81,82] I_{max} values followed the sensitivity rank, where the highest obtained sensitivities (650 nm to $Ag_{50}Au_{50}/SiO_2$ and 533/405 nm to $Ag_{79}Au_{21}$/GO) presented higher I_{max} values. K_m^{app} showed lower values for the experiments conducted with LSPR stimuli in comparison to dark conditions, indicating that LSPR could play a role in increasing the substrate affinity to the nanozymes. For both materials, K_m^{app} presented lower values for the experiments conducted with 405 nm. However, interestingly, I_{max} obtained at 405 nm for $Ag_{50}Au_{50}/SiO_2$ was 30% lower in comparison to the experiment performance with no LSPR stimulus. Following a similar bias, even though similar high sensitivities were found for 405 and 533 nm for $Ag_{79}Au_{21}$/GO, I_{max} showed a 40% lower value under 405 nm stimulus in comparison to the 533 nm. This result suggests that a laser source of higher energy may be the one to most interfere either in the reaction mechanism or stability of the system components.

The values found for sensitivity for both $Ag_{50}Au_{50}/SiO_2$ and $Ag_{79}Au_{21}$/GO are among the range described in the literature. Zhao et al. reported a summarized table of sensitivity values from different metal-containing composites for electrochemical H_2O_2 sensing, showing a range that, in general, varies from 22.27 to 396.7 μA mM^{-1} cm^{-2}.[79] Among 13 references

https://doi.org/10.1021/acsanm.1c02611
ACS Appl. Nano Mater. XXXX, XXX, XXX−XXX

brought in the survey, a single exception of PtNi supported on multiwalled carbon nanotubes showed a sensitivity of 2123.1 μA mM^{-1} cm^{-2}, being the only one to perform better than our best results after LSPR stimulus for both of our materials. Soto et al. developed an iron nanomaterial coated with graphene layers and supported on multiwalled carbon nanotubes, further deposited on a catalase functionalized electrode acting as a peroxidase for H_2O_2 sensing.[83] For this material, a sensitivity of 59 μA mM^{-1} cm^{-2} and a K_m^{app} value of 17.9 mM were found. Huang et al. determined a K_m^{app} of 2.81 mM for catalase in a gold NP-graphene composite.[84] Even the K_m^{app} of free catalase was determined to be 34.07 mM, demonstrating a much lower substrate affinity compared to our study with peroxidase-like nanozymes.[85] This outcome indicates that nanozymes have a vast potential to perform better than enzyme-based materials, with increased sensitivity and substrate affinity under Michaelis–Menten enzyme kinetics approach. Moreover, these parameters can be optimized after LSPR stimulus with the use of plasmonic nanoparticles.

Based on these results and the reported literature for the HPRR in alkaline media,[86−88] Scheme 2 suggests a mechanism

Scheme 2. Schematic Representation of the Hydrogen Peroxide Reduction Reaction in AgAu NS Under Light Irradiation in Alkaline Medium[a]

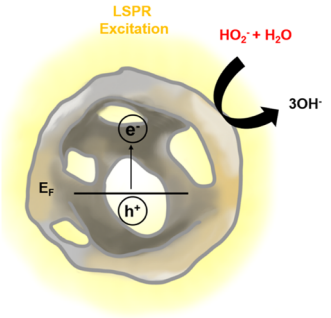

[a]The hot electrons generated flow to adsorbed HO_2^- ions, leading to its reduction and OH^- production.

for the plasmon-enhanced HPRR in AgAu NS supported on GO or SiO_2. As the support showed no catalytic contribution to the reaction, it was not considered in the scheme. As has been reported in the literature, the plasmon-enhanced HPRR leads to a kinetic improvement,[89−91] which has also been described for other plasmon-enhanced reactions. After hydrogen peroxide is added to the electrolyte, it is transformed into HO_2^- and dioxidanide, as its pKa (11.7) is lower than the pH of the electrolyte (pH = 13), as shown in eq 1.[86,87] Then, HO_2^- is adsorbed on the surface of the AgAu NS.[88] The dioxidanide is then reduced, leading to hydroxide ions. Under light irradiation, 533 or 650 nm for $Ag_{50}Au_{50}/SiO_2$ and $Ag_{79}Au_{21}$/GO, respectively, hot electrons and holes are generated from the LSPR of the AgAu NS and are injected into the dioxidanide, accelerating the electron transfer kinetics.[90]

The hot electrons are then transferred to dioxidanide, leading to the overall reduction of hydrogen peroxide (eq 2).

$$H_2O_2 + OH^- \rightleftharpoons HO_2^- + H_2O \quad (1)$$

$$HO_2^- + 2e^- + H_2O \rightleftharpoons 3OH^- \quad (2)$$

CONCLUSIONS

In summary, we have successfully developed an innovative synthesis in situ of AgAu bimetallic hollow nanostructures onto two different supports, GO and SiO_2. These structures presented different metallic ratios and, consequently, optical properties concerning the LSPR band shape and maximum. They were used as peroxidase-like nanozymes in the plasmon-enhanced HPRR for H_2O_2 electrochemical detection, in which their optimized performance regarding sensitivity was reached using laser matching of the wavelength at the maximum LSPR extinction of these structures. For $Ag_{79}Au_{21}$/GO, the sensitivity was improved by 122% at 533 nm and 105% at 405 nm compared to dark conditions, although almost no improvement (1.08%) was observed for the laser not matching the LSPR (650 nm). For $Ag_{50}Au_{50}/SiO_2$, the sensitivity was improved by 118% with exposure to the LSPR matching laser (650 nm) compared to dark conditions, although worse enhancements of 27% and 38% were obtained for the lasers not matching LSPR (405 and 533 nm, respectively). The materials presented high sensitivity values in comparison to previously reported nanozymes under dark conditions, which were optimized after LSPR stimulus. Under the Michaelis–Menten enzyme kinetics approach, I_{max} values for all experiments in both materials followed the same bias as sensitivity, reaching the highest values of 1177 μA cm^{-2} for $Ag_{50}Au_{50}/SiO_2$ upon 650 nm stimulus and 1405 μA cm^{-2} for $Ag_{79}Au_{21}$/GO upon 533 nm radiation. Both nanozymes presented lower K_m^{app} values in comparison to free catalase under dark conditions, indicating a high substrate affinity. These values were lowered after LSPR stimulus, especially upon 405 nm radiation, indicating better affinity than previously described enzymatic and nonenzymatic composites. The noticeable enhancement in the sensitivity, I_{max}, and K_m^{app} of sensors promoted by nanozymes suggests the efficacy of LSPR stimulus as an opportunity for the improvement of electrocatalytic reactions.

ASSOCIATED CONTENT

Supporting Information

The Supporting Information is available free of charge at https://pubs.acs.org/doi/10.1021/acsanm.1c02611.

Size distribution of AgNPs, AgAu NS, Ag in Ag/SiO_2 and Ag/GO, AgAu NS in $Ag_{50}Au_{50}/SiO_2$ and $Ag_{79}Au_{21}$/GO, and SiO_2 submicrospheres; TEM images of $Ag_{91}Au_{09}$ NS, $Ag_{77}Au_{23}$ NS, and $Ag_{50}Au_{50}$ NS; HRTEM and TEM-EDS characterization of AgAu NS; Raman spectrum of GO; XRD patterns of SiO_2 submicrospheres and GO; XPS data of $Ag_{50}Au_{50}/SiO_2$ and $Ag_{79}Au_{21}$/GO; cyclic voltammograms of SiO_2, GO, $Ag_{50}Au_{50}/SiO_2$, and $Ag_{79}Au_{21}$/GO; Nyquist plots for GO and SiO_2; chronoamperograms of $Ag_{50}Au_{50}/SiO_2$ and $Ag_{79}Au_{21}$/GO with and without light stimulus; and sensitivity bar graphs for GCE, GO, and SiO_2 (PDF)

AUTHOR INFORMATION

Corresponding Author

Susana I. Córdoba de Torresi − *Departamento de Química Fundamental, Instituto de Química, Universidade de São Paulo, São Paulo 05508-000, Brazil;* orcid.org/0000-0003-3290-172X; Email: storresi@iq.usp.br

https://doi.org/10.1021/acsanm.1c02611
ACS Appl. Nano Mater. XXXX, XXX, XXX−XXX

Authors

Rafael T. P. da Silva − *Departamento de Química Fundamental, Instituto de Química, Universidade de São Paulo, São Paulo 05508-000, Brazil;* orcid.org/0000-0002-1762-793X

Maria Paula de Souza Rodrigues − *Departamento de Química Fundamental, Instituto de Química, Universidade de São Paulo, São Paulo 05508-000, Brazil;* orcid.org/0000-0002-3731-2644

Gabriela F. B. Davilla − *Departamento de Química Fundamental, Instituto de Química, Universidade de São Paulo, São Paulo 05508-000, Brazil;* orcid.org/0000-0002-7545-2875

Adriano M. R. P. da Silva − *Departamento de Química Fundamental, Instituto de Química, Universidade de São Paulo, São Paulo 05508-000, Brazil;* orcid.org/0000-0002-9955-2571

André H. B. Dourado − *Nonequilibrium Chemical Physics, Department of Physics, Technische Universität München, 85748 Garching, Germany;* orcid.org/0000-0001-8354-6444

Complete contact information is available at: https://pubs.acs.org/10.1021/acsanm.1c02611

Author Contributions

R.T.P.S. and M.P.S.R. contributed equally. R.T.P.S., M.P.S.R., and S.I.C.T. conceived the project. R.T.P.S., G.F.B.D., and A.M.R.P.S. developed the AgAu/GO and AgAu/SiO_2 in situ synthesis and performed the material characterization. R.T.P.S. and M.P.S.R. developed and performed the plasmon-enhanced electrochemical assays and wrote the manuscript. A.H.B.D. performed and analyzed XPS data. S.I.C.T. supervised the work.

Notes

The authors declare no competing financial interest.

■ ACKNOWLEDGMENTS

This work was supported by CNPq (#302173/2016-1) and the São Paulo Research Foundation FAPESP (Grant Numbers 2015/26308-7 and 2018/16219-5). R.T.P.S. was funded by a PhD fellowship from CAPES (Grant 88882.328241/2019-01). M.P.S.R. was funded by a PhD fellowship from FAPESP (Grant Number 2018/16846-0).

■ ABBREVIATIONS

APTES, 3-aminopropylethoxysilane
ECSA, electrochemically active surface area
EDS, energy-dispersive spectroscopy
EIS, electrochemical impedance spectroscopy
GCE, glassy carbon electrode
GO, layered graphene oxide
GRR, galvanic replacement reaction
HPRR, hydrogen peroxide reduction reaction
LSPR, localized surface plasmon resonance
NIR, near-infrared
NP, nanoparticle
NS, nanoshell
SEM, scanning electron microscopy
SERS, surface-enhanced Raman spectroscopy
TEM, transmission electron microscopy
TEOS, tetraethyl orthosilicate
XPS, X-ray photoelectron spectroscopy
XRD, X-ray diffraction

■ REFERENCES

(1) Chen, S.; Yuan, R.; Chai, Y.; Hu, F. Electrochemical Sensing of Hydrogen Peroxide Using Metal Nanoparticles: A Review. *Microchim. Acta* **2013**, *180*, 15−32.

(2) Lu, W.; Luo, Y.; Chang, G.; Sun, X. Synthesis of Functional SiO2-Coated Graphene Oxide Nanosheets Decorated with Ag Nanoparticles for H2O2 and Glucose Detection. *Biosens. Bioelectron.* **2011**, *26*, 4791−4797.

(3) Sun, X.; Guo, S.; Liu, Y.; Sun, S. Dumbbell-like PtPd-Fe3O4 Nanoparticles for Enhanced Electrochemical Detection of H2O2. *Nano Lett.* **2012**, *12*, 4859−4863.

(4) Putt, K. S.; Pugh, R. B. A High-Throughput Microtiter Plate Based Method for the Determination of Peracetic Acid and Hydrogen Peroxide. *PLoS One* **2013**, *8*, No. e79218.

(5) Song, M.; Wang, J.; Chen, B.; Wang, L. A Facile, Nonreactive Hydrogen Peroxide (H2O2) Detection Method Enabled by Ion Chromatography with UV Detector. *Anal. Chem.* **2017**, *89*, 11537−11544.

(6) Hagen, C. L.; Sanders, S. T. Investigation of Multi-Species (H2O2 and H2O) Sensing and Thermometry in an HCCI Engine by Wavelength-Agile Absorption Spectroscopy. *Meas. Sci. Technol.* **2007**, *18*, 1992−1998.

(7) Teodoro, K. B. R.; Migliorini, F. L.; Christinelli, W. A.; Correa, D. S. Detection of Hydrogen Peroxide (H2O2) Using a Colorimetric Sensor Based on Cellulose Nanowhiskers and Silver Nanoparticles. *Carbohydr. Polym.* **2019**, *212*, 235−241.

(8) Wu, H.; Nißler, R.; Morris, V.; Herrmann, N.; Hu, P.; Jeon, S. J.; Kruss, S.; Giraldo, J. P. Monitoring Plant Health with Near-Infrared Fluorescent H2O2 Nanosensors. *Nano Lett.* **2020**, *20*, 2432−2442.

(9) Han, Y.; Zheng, J.; Dong, S. A Novel Nonenzymatic Hydrogen Peroxide Sensor Based on Ag-MnO2-MWCNTs Nanocomposites. *Electrochim. Acta* **2013**, *90*, 35−43.

(10) Chakraborty, S.; Retna Raj, C. Pt Nanoparticle-Based Highly Sensitive Platform for the Enzyme-Free Amperometric Sensing of H2O2. *Biosens. Bioelectron.* **2009**, *24*, 3264−3268.

(11) Thatikayala, D.; Ponnamma, D.; Sadasivuni, K. K.; Cabibihan, J.-J.; Al-Ali, A. K.; Malik, R. A.; Min, B. Progress of Advanced Nanomaterials in the Non-Enzymatic Electrochemical Sensing of Glucose and H2O2. *Biosensors* **2020**, *10*, No. 151.

(12) Chen, W.; Cai, S.; Ren, Q.-Q.; Wen, W.; Zhao, Y.-D. Recent Advances in Electrochemical Sensing for Hydrogen Peroxide: A Review. *Analyst* **2012**, *137*, 49−58.

(13) Dhara, K.; Mahapatra, D. R. Recent Advances in Electrochemical Nonenzymatic Hydrogen Peroxide Sensors Based on Nanomaterials: A Review. *J. Mater. Sci.* **2019**, *54*, 12319−12357.

(14) Pundir, C. S.; Deswal, R.; Narwal, V. Quantitative Analysis of Hydrogen Peroxide with Special Emphasis on Biosensors. *Bioprocess Biosyst. Eng.* **2018**, *41*, 313−329.

(15) Xu, F.; Sun, Y.; Zhang, Y.; Shi, Y.; Wen, Z.; Li, Z. Graphene-Pt Nanocomposite for Nonenzymatic Detection of Hydrogen Peroxide with Enhanced Sensitivity. *Electrochem. Commun.* **2011**, *13*, 1131−1134.

(16) Liang, M.; Yan, X. Nanozymes: From New Concepts, Mechanisms, and Standards to Applications. *Acc. Chem. Res.* **2019**, *52*, 2190−2200.

(17) Wang, H.; Gu, X.-K.; Zheng, X.; Pan, H.; Zhu, J.; Chen, S.; Cao, L.; Li, W.-X.; Lu, J. Disentangling the Size-Dependent Geometric and Electronic Effects of Palladium Nanocatalysts beyond Selectivity. *Sci. Adv.* **2019**, *5*, No. eaat6413.

(18) Roduner, E. Size Matters: Why Nanomaterials Are Different. *Chem. Soc. Rev.* **2006**, *35*, 583−592.

(19) Baffou, G.; Quidant, R. Nanoplasmonics for Chemistry. *Chem. Soc. Rev.* **2014**, *43*, 3898.

(20) Araujo, T. P.; Quiroz, J.; Barbosa, E. C. M.; Camargo, P. H. C. Understanding Plasmonic Catalysis with Controlled Nanomaterials Based on Catalytic and Plasmonic Metals. *Curr. Opin. Colloid Interface Sci.* **2019**, *39*, 110−122.

https://doi.org/10.1021/acsanm.1c02611
ACS Appl. Nano Mater. XXXX, XXX, XXX−XXX

(21) Huang, X.; Jain, P. K.; El-Sayed, I. H.; El-Sayed, M. A. Plasmonic Photothermal Therapy (PPTT) Using Gold Nanoparticles. *Lasers Med. Sci.* **2008**, *23*, 217−228.
(22) Jeon, T. Y.; Kim, D. H. J.; Park, S. G.; Kim, S. H.; Kim, D. H. J. Nanostructured Plasmonic Substrates for Use as SERS Sensors. *Nano Convergence* **2016**, *3*, No. 18.
(23) Ma, J.; Liu, X.; Wang, R.; Zhang, J.; Jiang, P.; Wang, Y.; Tu, G. Bimetallic Core-Shell Nanostars with Tunable Surface Plasmon Resonance for Surface-Enhanced Raman Scattering. *ACS Appl. Nano Mater.* **2020**, *3*, 10885−10894.
(24) Maji, S. K. Plasmon-Enhanced Electrochemical Biosensing of Hydrogen Peroxide from Cancer Cells by Gold Nanorods. *ACS Appl. Nano Mater.* **2019**, *2*, 7162−7169.
(25) Liu, W.; Wu, X.; Li, X. Gold Nanorods on Three-Dimensional Nickel Foam: A Non-Enzymatic Glucose Sensor with Enhanced Electro-Catalytic Performance. *RSC Adv.* **2017**, *7*, 36744−36749.
(26) Kabashin, A. V.; Evans, P.; Pastkovsky, S.; Hendren, W.; Wurtz, G. A.; Atkinson, R.; Pollard, R.; Podolskiy, V. A.; Zayats, A. V. Plasmonic Nanorod Metamaterials for Biosensing. *Nat. Mater.* **2009**, *8*, 867−871.
(27) Rycenga, M.; Cobley, C. M.; Zeng, J.; Li, W.; Moran, C. H.; Zhang, Q.; Qin, D.; Xia, Y. Controlling the Synthesis and Assembly of Silver Nanostructures for Plasmonic Applications. *Chem. Rev.* **2011**, *111*, 3669−3712.
(28) Achermann, M. Exciton-Plasmon Interactions in Metal-Semiconductor Nanostructures. *J. Phys. Chem. Lett.* **2010**, *1*, 2837−2843.
(29) Kisukuri, C. M.; Palmeira, D. J.; Rodrigues, T. S.; Camargo, P. H. C.; Andrade, L. H. Bimetallic Nanoshells as Platforms for Metallo- and Biometallo-Catalytic Applications. *ChemCatChem* **2016**, *8*, 171−179.
(30) Wang, J. L.; Ando, R. A.; Camargo, P. H. C. Investigating the Plasmon-Mediated Catalytic Activity of Agau Nanoparticles as a Function of Composition: Are Two Metals Better than One? *ACS Catal.* **2014**, *4*, 3815−3819.
(31) da Silva, A. G. M.; Rodrigues, T. S.; Correia, V. G.; Alves, T. V.; Alves, R. S.; Ando, R. A.; Ornellas, F. R.; Wang, J.; Andrade, L. H.; Camargo, P. H. C. Plasmonic Nanorattles as Next-Generation Catalysts for Surface Plasmon Resonance-Mediated Oxidations Promoted by Activated Oxygen. *Angew. Chem., Int. Ed.* **2016**, *55*, 7111−7115.
(32) Rodrigues, T. S.; da Silva, A. G. M.; de Moura, A. B. L.; Freitas, I. G.; Camargo, P. H. C. C. Rational Design of Plasmonic Catalysts: Matching the Surface Plasmon Resonance with Lamp Emission Spectra for Improved Performance in AgAu Nanorings. *RSC Adv.* **2016**, *6*, 62286−62290.
(33) Wang, N.; Cao, P.; Sun, S.; Ma, H.; Ma, H. Hollow Multiple Noble Metallic Nanoalloys by Mercury-Assisted Galvanic Replacement Reaction for Hydrogen Evolution. *Inorg. Chem.* **2021**, *60*, 3471−3478.
(34) Wang, H.; Zhao, W.; Zhao, Y.; Xu, C. H.; Xu, J. J.; Chen, H. Y. Real-Time Tracking the Electrochemical Synthesis of Au@Metal Core-Shell Nanoparticles toward Photo Enhanced Methanol Oxidation. *Anal. Chem.* **2020**, *92*, 14006−14011.
(35) Kisukuri, C. M.; Macedo, A.; Oliveira, C. C. S.; Camargo, P. H. C.; Andrade, L. H.; Prof, A.; Prestes, L.; Sa, S. P. Investigating the Influence of the Interface in Thiol-Functionalized Silver − Gold Nanoshells over Lipase Activity. *Langmuir* **2013**, *29*, 15974−15980.
(36) Genç, A.; Patarroyo, J.; Sancho-Parramon, J.; Bastús, N. G.; Puntes, V.; Arbiol, J. Hollow Metal Nanostructures for Enhanced Plasmonics: Synthesis, Local Plasmonic Properties and Applications. *Nanophotonics* **2017**, *6*, 193−213.
(37) Russo, L.; Merkoçi, F.; Patarroyo, J.; Piella, J.; Merkoçi, A.; Bastús, N. G.; Puntes, V. Time- and Size-Resolved Plasmonic Evolution with Nm Resolution of Galvanic Replacement Reaction in AuAg Nanoshells Synthesis. *Chem. Mater.* **2018**, *30*, 5098−5107.
(38) Vongsavat, V.; Vittur, B. M.; Bryan, W. W.; Kim, J. H.; Lee, T. R. Ultrasmall Hollow Gold-Silver Nanoshells with Extinctions Strongly Red-Shifted to the near-Infrared. *ACS Appl. Mater. Interfaces* **2011**, *3*, 3616−3624.
(39) Yan, X.; Yu, S.; Tang, Y.; Sun, D.; Xu, L.; Xue, C. Triangular AgAu@Pt Core−Shell Nanoframes with a Dendritic Pt Shell and Enhanced Electrocatalytic Performance toward the Methanol Oxidation Reaction. *Nanoscale* **2018**, *10*, 2231−2235.
(40) Saw, E. N.; Grasmik, V.; Rurainsky, C.; Epple, M.; Tschulik, K. Electrochemistry at Single Bimetallic Nanoparticles - Using Nano Impacts for Sizing and Compositional Analysis of Individual AgAu Alloy Nanoparticles. *Faraday Discuss.* **2016**, *193*, 327−338.
(41) Balasubramanian, P.; He, S.-B.; Jansirani, A.; Peng, H.-P.; Huang, L.-L.; Deng, H.-H.; Chen, W. Bimetallic AgAu Decorated MWCNTs Enable Robust Nonenzyme Electrochemical Sensors for In-Situ Quantification of Dopamine and H2O2 Biomarkers Expelled from PC-12 Cells. *J. Electroanal. Chem.* **2020**, *878*, No. 114554.
(42) Nazir, R.; Fageria, P.; Basu, M.; Pande, S. Decoration of Carbon Nitride Surface with Bimetallic Nanoparticles (Ag/Pt, Ag/Pd, and Ag/Au) via Galvanic Exchange for Hydrogen Evolution Reaction. *J. Phys. Chem. C* **2017**, *121*, 19548−19558.
(43) Hemmingson, S. L.; Campbell, C. T. Trends in Adhesion Energies of Metal Nanoparticles on Oxide Surfaces: Understanding Support Effects in Catalysis and Nanotechnology. *ACS Nano* **2017**, *11*, 1196−1203.
(44) Baek, S. H.; Roh, J.; Park, C. Y.; Kim, M. W.; Shi, R.; Kailasa, S. K.; Park, T. J. Cu-Nanoflower Decorated Gold Nanoparticles-Graphene Oxide Nanofiber as Electrochemical Biosensor for Glucose Detection. *Mater. Sci. Eng. C* **2020**, *107*, No. 110273.
(45) Shetti, N. P.; Malode, S. J.; Nayak, D. S.; Bagihalli, G. B.; Reddy, K. R.; Ravindranadh, K.; Reddy, C. V. A Novel Biosensor Based on Graphene Oxide-Nanoclay Hybrid Electrode for the Detection of Theophylline for Healthcare Applications. *Microchem. J.* **2019**, *149*, No. 103985.
(46) Dinesh, B.; Mani, V.; Saraswathi, R.; Chen, S. M. Direct Electrochemistry of Cytochrome c Immobilized on a Graphene Oxide-Carbon Nanotube Composite for Picomolar Detection of Hydrogen Peroxide. *RSC Adv.* **2014**, *4*, 28229−28237.
(47) Rossi, L. M.; Shi, L.; Quina, F. H.; Rosenzweig, Z. Stöber Synthesis of Monodispersed Luminescent Silica Nanoparticles for Bioanalytical Assays. *Langmuir* **2005**, *21*, 4277−4280.
(48) Liberman, A.; Mendez, N.; Trogler, W. C.; Kummel, A. C. Synthesis and Surface Functionalization of Silica Nanoparticles for Nanomedicine. *Surf. Sci. Rep.* **2014**, *69*, 132−158.
(49) Jeelani, P. G.; Mulay, P.; Venkat, R.; Ramalingam, C. Multifaceted Application of Silica Nanoparticles. A Review. *Silicon* **2020**, *12*, 1337−1354.
(50) Chastian, J. *Handbook of X-Ray Photoelectron Spectroscopy*; In Muilenberg, G. E., Ed.; Perkin Elmer Corporation: Eden Prairie, 1992.
(51) Yumitori, S. Correlation of C1s Chemical State Intensities with the O1s Intensity in the XPS Analysis of Anodically Oxidized Glass-like Carbon Samples. *J. Mater. Sci.* **2000**, *35*, 139−146.
(52) Papa, L.; de Freitas, I. C.; Geonmonond, R. S.; de Aquino, C. B.; Pieretti, J. C.; Domingues, S. H.; Ando, R. A.; Camargo, P. H. C. C. Supports Matter: Unraveling the Role of Charge Transfer in the Plasmonic Catalytic Activity of Silver Nanoparticles. *J. Mater. Chem. A* **2017**, *5*, 11720−11729.
(53) Marcano, D. C.; Kosynkin, D. V.; Berlin, J. M.; Sinitskii, A.; Sun, Z.; Slesarev, A.; Alemany, L. B.; Lu, W.; Tour, J. M. Improved Synthesis of Graphene Oxide. *ACS Nano* **2010**, *4*, 4806−4814.
(54) Jacinto, M. J.; Kiyohara, P. K.; Masunaga, S. H.; Jardim, R. F.; Rossi, L. M. Recoverable Rhodium Nanoparticles: Synthesis, Characterization and Catalytic Performance in Hydrogenation Reactions. *Appl. Catal., A* **2008**, *338*, 52−57.
(55) Xia, X.; Wang, Y.; Ruditskiy, A.; Xia, Y. 25th Anniversary Article: Galvanic Replacement: A Simple and Versatile Route to Hollow Nanostructures with Tunable and Well-Controlled Properties. *Adv. Mater.* **2013**, *25*, 6313−6333.
(56) Wang, Y.; Wan, D.; Xie, S.; Xia, X.; Huang, C. Z.; Xia, Y. Synthesis of Silver Octahedra with Controlled Sizes and Optical

https://doi.org/10.1021/acsanm.1c02611
ACS Appl. Nano Mater. XXXX, XXX, XXX−XXX

Properties via Seed-Mediated Growth. *ACS Nano* **2013**, *7*, 4586−4594.
(57) Gilroy, K. D.; Ruditskiy, A.; Peng, H. C.; Qin, D.; Xia, Y. Bimetallic Nanocrystals: Syntheses, Properties, and Applications. *Chem. Rev.* **2016**, *116*, 10414−10472.
(58) Pansare, V. J.; Hejazi, S.; Faenza, W. J.; Prud'homme, R. K. Review of Long-Wavelength Optical and NIR Imaging Materials: Contrast Agents, Fluorophores, and Multifunctional Nano Carriers. *Chem. Mater.* **2012**, *24*, 812−827.
(59) Gao, L.; Liu, R.; Gao, F.; Wang, Y.; Jiang, X.; Gao, X. Plasmon-Mediated Generation of Reactive Oxygen Species from near-Infrared Light Excited Gold Nanocages for Photodynamic Therapy in Vitro. *ACS Nano* **2014**, *8*, 7260−7271.
(60) Enrichi, F.; Quandt, A.; Righini, G. C. Plasmonic Enhanced Solar Cells: Summary of Possible Strategies and Recent Results. *Renewable Sustainable Energy Rev.* **2018**, *82*, 2433−2439.
(61) Rao, X.; Tatoulian, M.; Guyon, C.; Ognier, S.; Chu, C.; Hassan, A. A. A Comparison Study of Functional Groups (Amine vs. Thiol) for Immobilizing AuNPs on Zeolite Surface. *Nanomaterials* **2019**, *9*, No. 1034.
(62) Sarkar, S. K.; Raul, K. K.; Pradhan, S. S.; Basu, S.; Nayak, A. Magnetic Properties of Graphite Oxide and Reduced Graphene Oxide. *Physica E* **2014**, *64*, 78−82.
(63) Siburian, R.; Sihotang, H.; Lumban Raja, S.; Supeno, M.; Simanjuntak, C. New Route to Synthesize of Graphene Nano Sheets. *Orient. J. Chem.* **2018**, *34*, 182−187.
(64) Johra, F. T.; Lee, J. W.; Jung, W. G. Facile and Safe Graphene Preparation on Solution Based Platform. *J. Ind. Eng. Chem.* **2014**, *20*, 2883−2887.
(65) Zhidkov, I. S.; Kurmaev, E. Z.; Condorelli, M.; Cholakh, S. O.; Boyarchenkov, A. S.; Fazio, E.; D'urso, L. X-Ray Photoelectron Spectra of Ag-Au Colloidal Nanoparticles after Interaction with Linear Carbon Chains. *Appl. Sci.* **2021**, *11*, No. 685.
(66) Jeon, T. H.; Monllor−Satoca, D.; Moon, G. −H.; Kim, W.; Kim, H. −I.; Bahnemann, D. W.; Park, H.; Choi, W. Ag(I) Ions Working as a Hole-Transfer Mediator in Photoelectrocatalytic Water Oxidation on WO3 Film. *Nat. Commun.* **2020**, *11*, No. 967.
(67) Sankar, M.; He, Q.; Morad, M.; Pritchard, J.; Freakley, S. J.; Edwards, J. K.; Taylor, S. H.; Morgan, D. J.; Carley, A. F.; Knight, D. W.; Kiely, C. J.; Hutchings, G. J. Synthesis of Stable Ligand-Free Gold-Palladium Nanoparticles Using a Simple Excess Anion Method. *ACS Nano* **2012**, *6*, 6600−6613.
(68) Radnik, J.; Mohr, C.; Claus, P. On the Origin of Binding Energy Shifts of Core Levels of Supported Gold Nanoparticles and Dependence of Pretreatment and Material Synthesis. *Phys. Chem. Chem. Phys.* **2003**, *5*, 172−177.
(69) Ding, R.; Qi, L.; Jia, M.; Wang, H. Simple Hydrothermal Synthesis of Mesoporous Spinel NiCo2O4 Nanoparticles and Their Catalytic Behavior in CH3OH Electro-Oxidation and H2O2 Electro-Reduction. *Catal. Sci. Technol.* **2013**, *3*, 3207−3215.
(70) Li, Y.; Cao, D.; Liu, Y.; Liu, R.; Yang, F.; Yin, J.; Wang, G. CuO Nanosheets Grown on Cupper Foil as the Catalyst for H 2O 2 Electroreduction in Alkaline Medium. *Int. J. Hydrogen Energy* **2012**, *37*, 13611−13615.
(71) Ensafi, A. A.; Zandi-Atashbar, N.; Rezaei, B.; Ghiaci, M.; Taghizadeh, M. Silver Nanoparticles Decorated Carboxylate Functionalized SiO2, New Nanocomposites for Non-Enzymatic Detection of Glucose and Hydrogen Peroxide. *Electrochim. Acta* **2016**, *214*, 208−216.
(72) Yin, J.; Qi, X.; Yang, L.; Hao, G.; Li, J.; Zhong, J. A Hydrogen Peroxide Electrochemical Sensor Based on Silver Nanoparticles Decorated Silicon Nanowire Arrays. *Electrochim. Acta* **2011**, *56*, 3884−3889.
(73) Chang, B. Y.; Park, S. M. Electrochemical Impedance Spectroscopy. *Annu. Rev. Anal. Chem.* **2010**, *3*, 207−229.
(74) Lasia, A. Electrochemical Impedance Spectroscopy and Its Applications. In *Modern Aspects of Electrochemistry*; Springer: Boston, MA, 2002; Vol. *32*, pp 143−248.
(75) Wu, Z. L.; Li, C. K.; Yu, J. G.; Chen, X. Q. MnO2/Reduced Graphene Oxide Nanoribbons: Facile Hydrothermal Preparation and Their Application in Amperometric Detection of Hydrogen Peroxide. *Sens. Actuators, B* **2017**, *239*, 544−552.
(76) Pan, Y.; Hou, Z.; Yi, W.; Zhu, W.; Zeng, F.; Liu, Y. N. Hierarchical Hybrid Film of MnO2 Nanoparticles/Multi-Walled Fullerene Nanotubes-Graphene for Highly Selective Sensing of Hydrogen Peroxide. *Talanta* **2015**, *141*, 86−91.
(77) Munawar, K.; Mansoor, M. A.; Olmstead, M. M.; Zaharinie, T.; Mohd Zubir, M. N.; Haniffa, M.; Basirun, W. J.; Mazhar, M. Fabrication of Ag-ZnO Composite Thin Films for Plasmonic Enhanced Water Splitting. *Mater. Chem. Phys.* **2020**, *255*, No. 123220.
(78) Yang, C.; Cattelan, M.; Fox, N.; Huang, Y.; Golden, M. S.; Schwarzacher, W. Electrochemical Modification and Characterization of Topological Insulator Single Crystals. *Langmuir* **2019**, *35*, 2983−2988.
(79) Zhao, W.; Jin, J.; Wu, H.; Wang, S.; Fneg, C.; Yang, S.; Ding, Y. Electrochemical Hydrogen Peroxide Sensor Based on Carbon Supported Cu@Pt Core-Shell Nanoparticles. *Mater. Sci. Eng. C* **2017**, *78*, 185−190.
(80) Jiang, B.; Duan, D.; Gao, L.; Zhou, M.; Fan, K.; Tang, Y.; Xi, J.; Bi, Y.; Tong, Z.; Gao, G. F.; Xie, N.; Tang, A.; Nie, G.; Liang, M.; Yan, X. Standardized Assays for Determining the Catalytic Activity and Kinetics of Peroxidase-like Nanozymes. *Nat. Protoc.* **2018**, *13*, 1506−1520.
(81) Anusha, J. R.; Raj, C. J.; Cho, B. B.; Fleming, A. T.; Yu, K. H.; Kim, B. C. Amperometric Glucose Biosensor Based on Glucose Oxidase Immobilized over Chitosan Nanoparticles from Gladius of Uroteuthis Duvauceli. *Sens. Actuators, B* **2015**, *215*, 536−543.
(82) Ramanavičius, A.; Kaušaite, A.; Ramanavičiene, A. Polypyrrole-Coated Glucose Oxidase Nanoparticles for Biosensor Design. *Sens. Actuators, B* **2005**, *111−112*, 532−539.
(83) Soto, D.; Alzate, M.; Gallego, J.; Orozco, J. Hybrid Nanomaterial/Catalase-Modified Electrode for Hydrogen Peroxide Sensing. *J. Electroanal. Chem.* **2021**, *880*, No. 114826.
(84) Huang, K. J.; Niu, D. J.; Liu, X.; Wu, Z. W.; Fan, Y.; Chang, Y. F.; Wu, Y. Y. Direct Electrochemistry of Catalase at Amine-Functionalized Graphene/Gold Nanoparticles Composite Film for Hydrogen Peroxide Sensor. *Electrochim. Acta* **2011**, *56*, 2947−2953.
(85) Prakash, P. A.; Yogeswaran, U.; Chen, S. M. A Review on Direct Electrochemistry of Catalase for Electrochemical Sensors. *Sensors* **2009**, *9*, 1821−1844.
(86) Poux, T.; Bonnefont, A.; Ryabova, A.; Kéranguéven, G.; Tsirlina, G. A.; Savinova, E. R. Electrocatalysis of Hydrogen Peroxide Reactions on Perovskite Oxides: Experiment versus Kinetic Modeling. *Phys. Chem. Chem. Phys.* **2014**, *16*, 13595−13600.
(87) Cai, X.; Tanner, E. E. L.; Lin, C.; Ngamchuea, K.; Foord, J. S.; Compton, R. G. The Mechanism of Electrochemical Reduction of Hydrogen Peroxide on Silver Nanoparticles. *Phys. Chem. Chem. Phys.* **2018**, *20*, 1608−1614.
(88) Strbac, S. The Effect of PH on Oxygen and Hydrogen Peroxide Reduction on Polycrystalline Pt Electrode. *Electrochim. Acta* **2011**, *56*, 1597−1604.
(89) Zhao, X.; Deng, Z.; Zhao, W.; Feng, B.; Wang, M.; Huang, M.; Liu, L.; Zou, G.; Shao, Y.; Zhu, H. Nanoporous Silver Using Pulsed Laser Deposition for High-Performance Oxygen Reduction Reaction and Hydrogen Peroxide Sensing. *Nanoscale* **2020**, *12*, 19413−19419.
(90) Maduraiveeran, G.; et al. Electrochemical Detection of Hydrogen Peroxide Based on Silver Nanoparticles via Amplified Electron Transfer Process. *J. Mater. Sci.* **2018**, *53*, 8328−8338.
(91) Silva, C. G.; Juárez, R.; et al. Influence of Excitation Wavelength (UV or Visible Light) on the Photocatalytic Activity of Titania Containing Gold Nanoparticles for the Generation of Hydrogen or Oxygen. *J. Am. Chem. Soc.* **2011**, *22*, 595−602.

https://doi.org/10.1021/acsanm.1c02611
ACS Appl. Nano Mater. XXXX, XXX, XXX−XXX